LANGMUIR

pubs.acs.org/Langmuir Article

Simultaneous Decomposition and Dewetting of Nanoscale Alloys: A Comparison of Experiment and Theory

Javier A. Diez, Alejandro G. González, David A. Garfinkel, Philip D. Rack, Joseph T. McKeown, and Lou Kondic*

Cite This: *Langmuir* 2021, 37, 2575−2585 Read Online

ACCESS | Metrics & More | Article Recommendations | Supporting Information

ABSTRACT: We consider the coupled process of phase separation and dewetting of metal alloys of nanoscale thickness deposited on solid substrates. The experiments involve applying nanosecond laser pulses that melt the $Ag_{40}Ni_{60}$ alloy films in two setups: either on thin supporting membranes or on bulk substrates. These two setups allow for extracting both temporal and spatial scales on which the considered processes occur. The theoretical model involves a longwave version of the Cahn−Hilliard formulation used to describe spinodal decomposition, coupled with an asymptotically consistent longwave-based description of dewetting that occurs due to destabilizing interactions between the alloy and the substrate, modeled using the disjoining pressure approach. Careful modeling, combined with linear stability analysis and fully nonlinear simulations, leads to results consistent with the experiments. In particular, we find that the two instability mechanisms occur concurrently, with the phase separation occurring faster and on shorter temporal scales. The modeling results show a strong influence of the temperature dependence of relevant material properties, implying that such a dependence is crucial for the understanding of the experimental findings. The agreement between theory and experiment suggests the utility of the proposed theoretical approach in helping to develop further experiments directed toward formation of metallic alloy nanoparticles of desired properties.

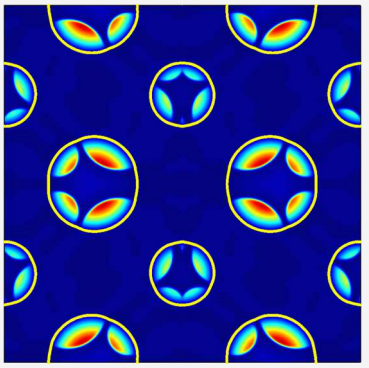

INTRODUCTION

Metal films of nanoscale thickness deposited on solid substrates and exposed to laser pulses melt and dewet into nanoparticle arrays, which find applications in a number of different fields including solar cells, plasmonics, sensors, and detectors, among others; see refs 1, 2 for recent reviews. In addition to the basic scientific interest, understanding of these interface-driven instabilities is further motivated by their potential to drive various self- and directed-assembly mechanisms.[3,4] In the past decade, experimental techniques have improved significantly, which lay the foundation for new theoretical insights into the dynamics of pure metals and also bilayer films.[5−7] However, there has been very limited experimental work on immiscible systems going through phase separation while being unstable with respect to the dewetting type of instability, see ref 3 and references therein. Such systems are of particular interest since they allow for multifunctional properties, associated with the multiple phases that emerge in the nanoparticle, to be realized.[8−12] From the theoretical point of view, the considered systems are challenging since they involve two coupled instability mechanisms operating in parallel. In addition, the presence of a substrate clearly influences the dewetting process and may also play a role in phase separation. Although models describing unstable multicomponent systems are available (e.g., Cahn−Hilliard formulation[13]), further work is needed to formulate a tractable formulation in particular when the domain of interest (the film itself) is evolving as well. We note that a film geometry (film between two substrates) was considered in refs 14, 15 including discussion of the boundary conditions between the film and the substrate. Phase separation was coupled to fluid dynamics in model-H; see refs 16, 17 for reviews. To describe coupling of dewetting and decomposition, model-H needs to be completed by boundary conditions; such a model was studied without dewetting but including the substrate and consideration of films with free surfaces.[18−20] Then, model-H was simplified in longwave approximation, considering also the coupling between decomposition and dewetting instability.[21,22] We are, however, not aware of any previous work applying these models to describe and model instabilities of films of nanoscale thickness in the context of a specific experiment.

This paper is organized as follows. First, we discuss two types of pulsed laser-induced dewetting (PLiD) experiments that provide complementary information about free surface and chemical phase-separation instabilities in the $Ag_{40}Ni_{60}$ system, where a liquid-phase miscibility gap exists below 2800 K: (i)

Received: October 14, 2020
Revised: January 24, 2021
Published: February 15, 2021

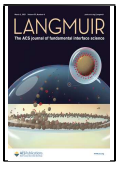

https://dx.doi.org/10.1021/acs.langmuir.0c02964
Langmuir 2021, 37, 2575−2585

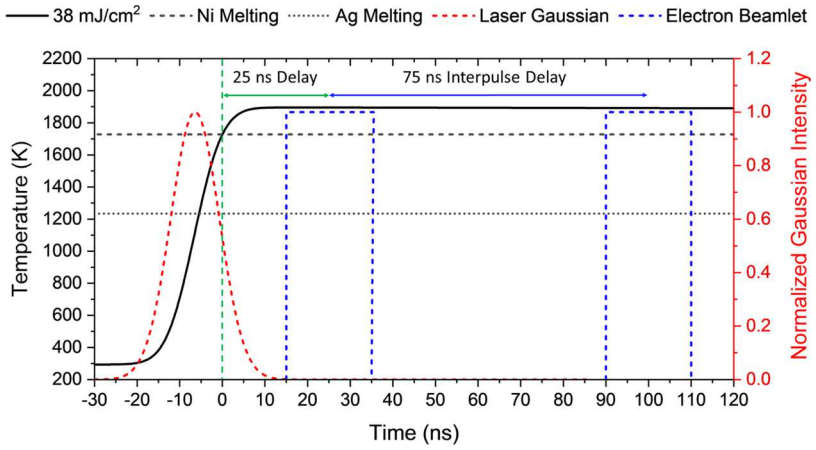

Figure 1. Finite-element method (FEM)-based temperature simulation of the $Ag_{40}Ni_{60}$ thin film DTEM experiment illustrating imaging at 25 and 100 ns liquid lifetimes. The red dashed curve is the normalized laser intensity, the solid black curve is the temperature profile of the $Ag_{40}Ni_{60}$ assuming a 38 mJ/cm^2 laser fluence, and the blue dashed square waves denote the electron beamlets. See Supporting Information Section 1 for more details on FEM simulations.

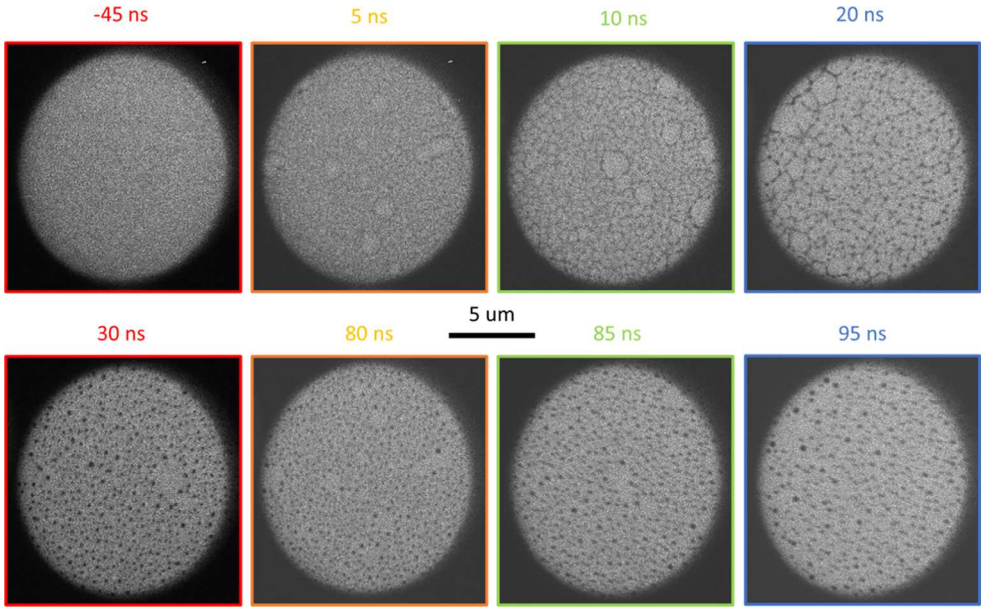

Figure 2. DTEM images of $Ag_{40}Ni_{60}$ thin film dewetting progression as a compilation of four separate experiments (denoted by image border color). The time is measured relative to the onset of Ni melting. The length of the horizontal black line corresponds to 5 μm.

experiments on thin supporting membranes that provide time-resolved information about free surface instability, as well as for long-time analysis of the chemical composition of the resulting nanoparticles and (ii) experiments carried out on bulk silicon that provide simultaneous information about both free surface and chemical instabilities, albeit with lower temporal resolution. Then, we discuss the theoretical model that we have further developed and adapted. As we will see, a direct connection between experiments and theory is insightful since the experimental results immediately justify the choice of material parameters in the model. We then proceed to discuss the results of linear stability analysis as well as of fully nonlinear time-dependent simulations that provide additional insight into the physical mechanisms governing the instabilities.

EXPERIMENTAL METHODS

Two different substrates were used in our experiments: (1) a thin 15 nm SiNx membrane supported at the perimeter with 200 μm thick Si and (2) 100 nm thermally grown SiO_2 on 500 μm Si "bulk" samples. $Ag_{40}Ni_{60}$ thin films were grown on both substrates via radio frequency magnetron cosputtering from individual Ag and Ni targets powered with 40 and 70 W, respectively. The as-deposited film forms as a supersaturated nanocrystalline solid solution[23] and is liquefied using nanosecond laser pulses.[23] The first set of experiments is carried out on thin membranes.[24,25] The experiments use dynamic transmission electron microscopy (DTEM) that offers the unique ability to resolve small-scale morphological changes on the nanosecond time scale during in situ photothermal heating. Thus, this technique allows for the direct determination of the metal liquid thin film free surface evolution. DTEM utilizes two pulsed lasers: one directed to the cathode to photoexcite an electron beamlet and a second directed at the substrate to photothermally heat the sample. The two laser sources are synchronized such that the imaging electrons arrive at various "delay" times relative to the heating pulse, and thus provide snapshots of the evolving system with nanosecond temporal resolution. For these experiments, the average laser fluence was 38 $\pm$ 1.5 mJ/cm^2 using a 1064 nm wavelength and a 12 ns (full width of the laser beam at $1/e^2$ of the maximum fluence) Gaussian laser profile and a 20 ns square wave

https://dx.doi.org/10.1021/acs.langmuir.0c02964
Langmuir 2021, 37, 2575−2585

electron beamlet with a 75 ns electron beamlet interpulse delay time (blue double arrow in Figure 1). The metal temperature after a single laser pulse computed using a finite-element method (FEM) for a stationary 10 nm $Ag_{40}Ni_{60}$ film on a 15 nm SiNx membrane is shown as well. FEM simulations, including discussion of the parameters entering the simulations, were described previously[23] (see also Supporting Information Section 1 for more details). The FEM result suggests that the temperature exceeds both the Ag (1234 K) and Ni (1728 K) melting temperatures, and thus, the film fully liquefies; furthermore, the high-temperature Ni melts ∼7 ns after the laser pulse peaks. Subsequently, the liquid state is maintained for long times (>1 μs) (such long times are not included in Figure 1). Figure 1 also shows the DTEM delay time (green double arrow), defined as the difference between the center of the imaging electron beamlet and the simulated time at which the film temperature reaches the Ni melting temperature. The latter time is for simplicity used as origin for the time axes. We note that since the electron beamlet used for imaging has a 20 ns pulse width, the information (about the laser pulse) ±10 ns from the times denoted contributions to the results.

The second experimental setup considers metal films on a bulk substrate, which is a much better heat sink, and thus requires higher laser fluence and yields significantly faster cooling rates. Thus a 248 nm KrF laser with a 20 ns Gaussian pulse width and a laser fluence of 170 mJ/cm^2 was used to perform PLiD on the bulk samples. The rapid cooling allows for subtle changes associated with the brief high-temperature liquid lifetime to be frozen into the microstructure and then characterized ex situ (Figure 4 later in the text includes the example of simulation results).

EXPERIMENTAL RESULTS

Before presenting the experimental results, it is instructed to first review the general dewetting dynamics that are observed in metallic thin films. A thin solid metal film, while not in its lowest energy state due to its high surface area to volume ratio, is typically stable at room temperature (on experimental time scales) since the requisite diffusive material transport is slow. When pulsed with a laser at a fluence sufficient to melt the film, the liquid film can dewet via spinodal dewetting or by nucleation of holes.[3] After a hole formation, the rim surrounding the hole expands, coalescing into a network of rivulets. These rivulets subsequently destabilize via the Rayleigh−Plateau type of instability into drops that solidify into truncated nanoparticles sitting on the substrate with wetting angles with the substrate governed by the balance of liquid metal−substrate−vacuum interface energies. In this work, we are interested in elucidating how these fluid instabilities and consequent material transport are affected via the simultaneous phase separation of an immiscible alloy. To accomplish this, we perform in situ DTEM experiments to determine the dewetting time scale and then compare results on bulk substrates where we can observe the resulting competition between the free surface instabilities and the phase separation. The sequence of images shown in Figure 2 is generated through the combination of four separate (PLiD/DTEM) experiments, with each experiment denoted by a specific color in the border of the images where two cathode pulses are generated for each experiment with an interpulse delay time of 75 ns (note the blue double arrow in Figure 1). Figure 2 shows the DTEM results demonstrating a progression from a 10 nm $Ag_{40}Ni_{60}$ thin film deposited on a thin Si_3N_4 membrane to an array of nanoparticles formed via PLiD. Changes to the sample morphology are observed after 5 ns, in the form of isolated hole formation. The film then progresses to partial breakup into rivulets at 20 ns and nanoparticles by 30 ns. These results are consistent with previous DTEM experiments.[24] We also note the similarity of the emerging patterns to the ones observed during dewetting of polymer films,[26−28] although the latter occur on very different time scales due to significantly larger viscosities.[3]

Beyond film breakup, we also observe phase separation in the resulting nanoparticles. Figure 3 illustrates a high-angle annular dark-field (HAADF) image and energy-dispersive X-ray spectroscopy maps of the combined Ag and Ni concentrations from the dewetted film. The HAADF images are generated from electrons scattered at high angles so

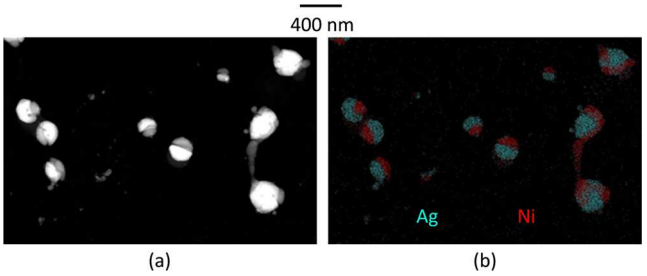

Figure 3. (a) High-angle annular dark-field (HAADF) scanning transmission electron image of AgNi nanoparticles and (b) energy-dispersive X-ray spectroscopy (EDS) image of (a) illustrating the chemical morphology of the resultant nanoparticles (where red denotes Ni and light blue denotes silver). Note that the results are long-time configurations, obtained after solidification that occurs on the microsecond time scale.

that they have both thickness and atomic number contrast. Thus, the larger particles appear brighter and for areas that are not saturated, the Ag is brighter than Ni. Several nanoparticle morphologies emerge, including bimetallic Janus nanoparticles, and for larger particles, we find Ni regions decorating the Ag core particles.

The competition between dewetting and phase separation was observed through PLiD experiments on a bulk substrate (Figures 4−6), where cooling times are much more rapid. Note that a higher fluence and slightly longer pulse width is used for the bulk substrate experiments. Figure 4 demonstrates a PLiD progression from one to five pulses for three different initial film thicknesses: (a) 10, (b) 20, and (c) 30 nm. Each image was taken near isolated hole formations, indicating that the film is in the initial stages of dewetting. Whereas dewetting was sufficiently slow in the thicker films (20 and 30 nm) to capture holes in the laser center, the 10 nm film produced fully formed nanoparticles in the laser center after one pulse. Thus, for the 10 nm film, images were taken just outside the laser hot spot to observe this same stage of dewetting. Also shown in Figure 4d are FEM simulations that indicate the rapid cooling associated with the 20 ns Gaussian laser pulse width. The liquid lifetime for the 10 nm $Ag_{40}Ni_{60}$ film determined through FEM simulations is ≈20 ns, which is consistent with the ≈30 ns evolution time determined in Figure 2.

Figure 4 demonstrates that there are obvious signs of phase separation for all film thicknesses after one laser pulse, as seen by the contrast in the film neighboring the holes. Here, Ag develops as the darker matrix of the microstructure and the Ni as the brighter islands. Further validation of chemical segregation, discussed below, indicates that phase separation starts developing prior to spinodal dewetting and that there is a coarsening observed for longer times (multiple laser pulses). The Ni lamella width in the 10 nm thick film is on the order of 9.2 ± 1.9 nm (24.7 ± 3.4 nm center-to-center spacing) and 15.8 ± 3.6 (42.0 ± 7.4 nm) for 1 pulse and 5 pulse samples, respectively. The corresponding results for thicker films can be seen in Figure 1 in the Supporting Information.

To verify the origin of the contrast occurring within the metal film, chemical analysis, via energy-dispersive X-ray spectroscopy (EDS), was performed. Figure 5a shows an scanning electron miscroscopy (SEM) image with an overlaid green arrow denoting the region where an EDS line scan was measured. Figure 5b illustrates the Ag and Ni composition along the green line shown in Figure 5a. The Ag and Ni concentrations fluctuate in a manner consistent with the contrast seen in the SEM image. To further validate that the contrast observed in Figure 4a−c can be attributed to chemical segregation, Figure 5d shows a two-dimensional map of Ag and Ni in the box selected in Figure 5c. Once again there is a correlation between chemical segregation, as demonstrated by the green (Ag) and red (Ni) regions in Figure 5d, and the contrast observed in Figure 5c.

The length scale of dewetting for a 10 nm film was determined by nearest-neighbor analysis of dewetted particles, as seen in Figure 6. The images were processed using ImageJ software. The contrast was optimized and the image was thresholded to generate a pure black and

https://dx.doi.org/10.1021/acs.langmuir.0c02964
Langmuir 2021, 37, 2575−2585

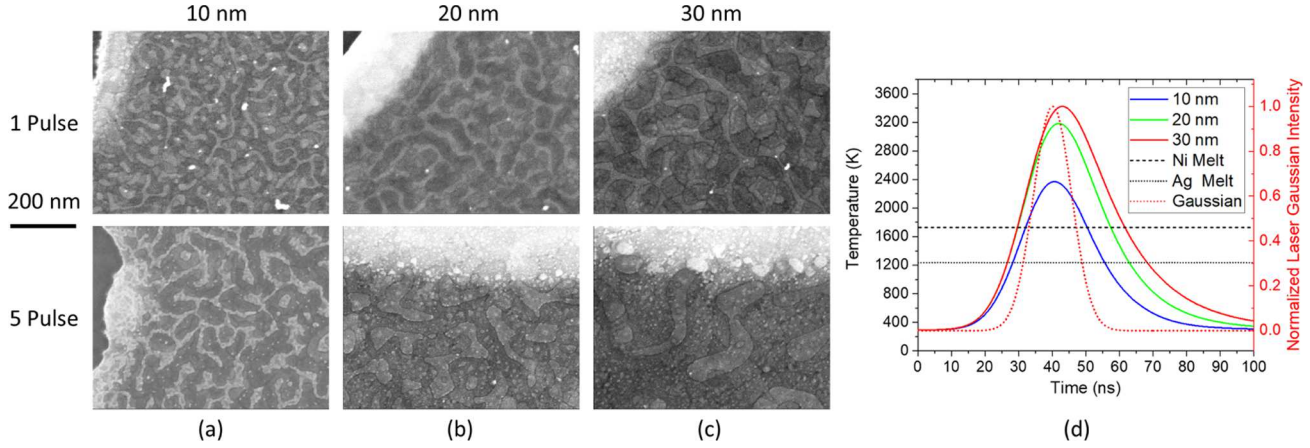

Figure 4. (a−c) Images of phase separation for films of thicknesses of 10, 20, and 30 nm and (d) FEM simulations for a single pulse for 10, 20, and 30 nm thick films. Note that the red dashed line is the normalized laser intensity (left axis) and the two horizontal dashed and dotted lines are the Ni and Ag melting temperatures, respectively.

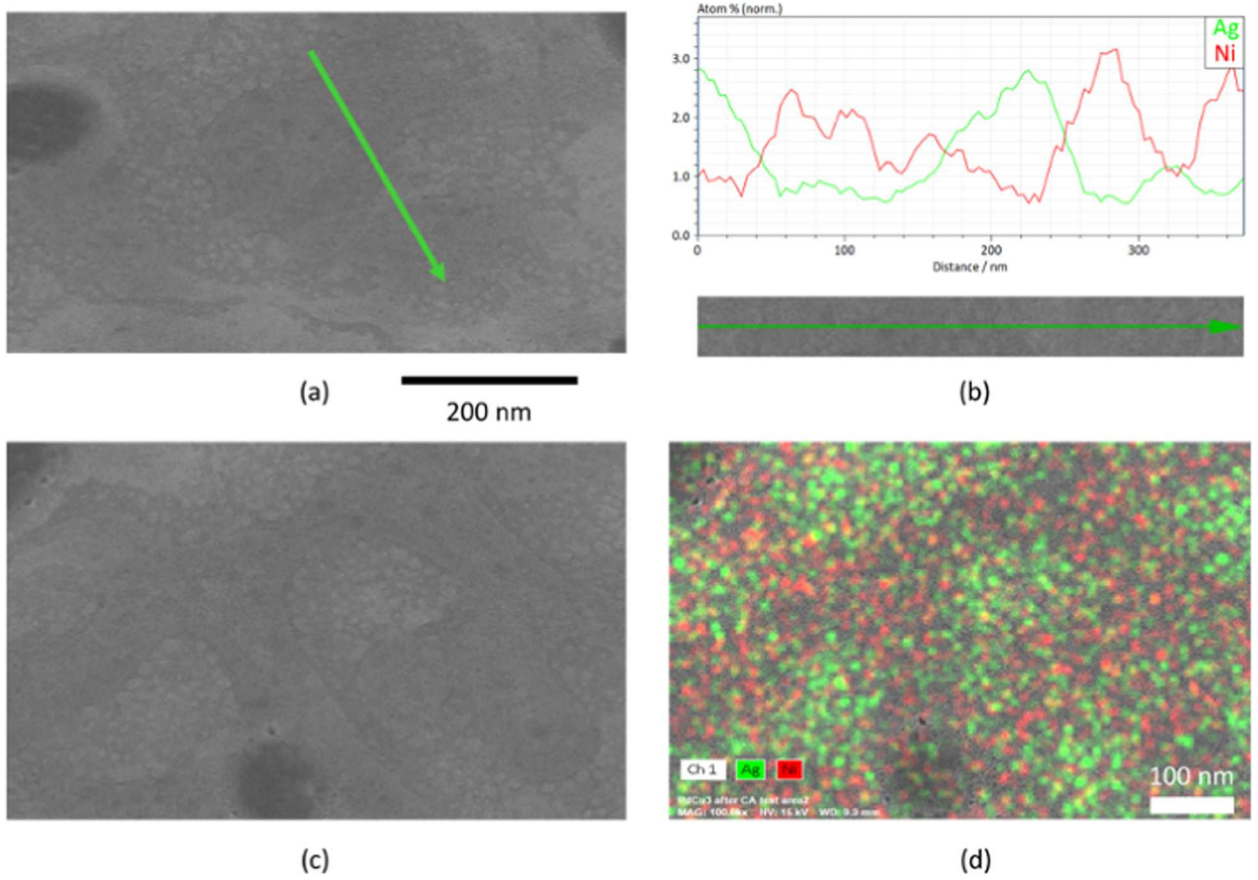

Figure 5. (a) SEM image of the 30 nm thick AgNi film following 20 pulses, (b) EDS line scan associated with (a), (c) SEM image of the 30 nm AgNi film following 20 pulses, and (d) EDS map of Ag (green) and Ni (red) associated with (c). Note that the parts (a) and (c) show different regions of the film.

white image. Subsequently, the average spacing was determined using the ImageJ nearest-neighbor plugin (NND), which generates a list of nearest-neighbor spacings for each particle. Figure 6a shows a SEM image of the dewetted film, and Figure 6b shows the nearest-neighbor distribution. Small areas of the part (Figure 6a) of the image were selected (Figure 6c,e), where the image is processed (Figure 6d,f) and analyzed to determine the nearest-neighbor distribution. The peak of this normal distribution (160−180 nm) is consistent with the average spacing (175 nm) determined from this distribution.

THEORETICAL MODELING

To model the presented experiments, we consider a thin nonvolatile film of a melted binary alloy on a solid substrate. While in general such a problem could be very complicated to model, within the longwave approach, significant simplifications could be reached; see refs 21, 29 for general formulation and refs 30, 31 for applications in the context of polymer−nanoparticle mixtures. As in these cases, our problem can be described by a gradient dynamics formulation. The equations that govern the

https://dx.doi.org/10.1021/acs.langmuir.0c02964
Langmuir 2021, 37, 2575−2585

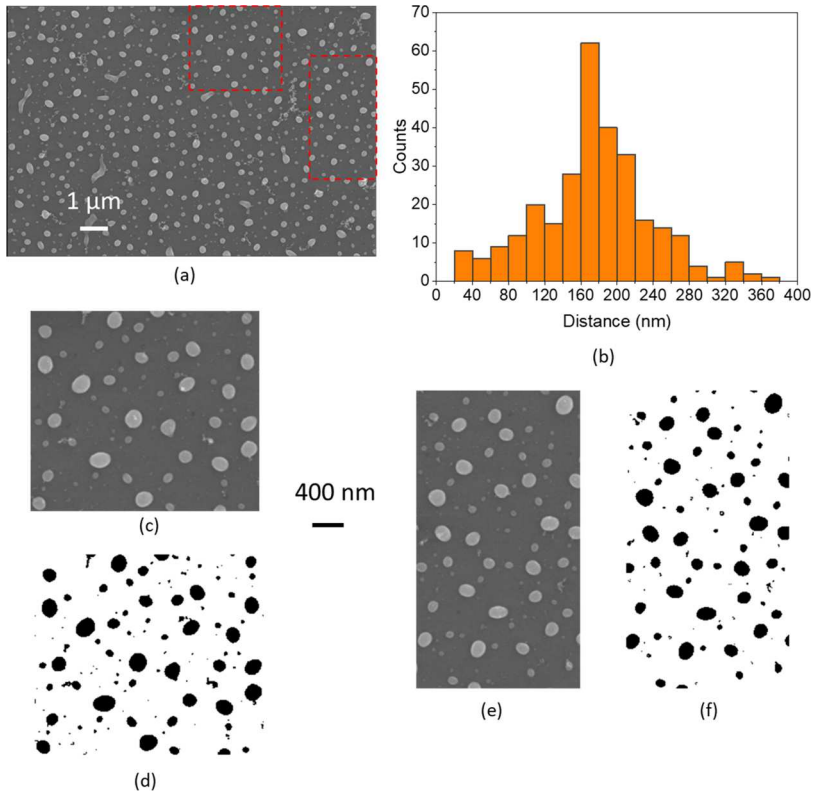

Figure 6. (a) SEM image of laser hot spot for the 10 nm sample after one pulse, (b) distribution of measured particle spacing from (a), and (c−f) examples of raw and processed selections from (a) for particle analysis.

progression to equilibrium can be deduced by considering the following free energy functional[22]

$$\mathcal{F} = \int \left[\gamma \left(1 + \frac{|\nabla h|^2}{2} \right) + \kappa F(\xi, \phi) + h\, \mathcal{E} G(\phi) + \sigma \frac{h|\nabla \phi|^2}{2} \right] \mathrm{d}A \tag{1}$$

where h and ϕ are the film thickness and the height-averaged per volume solute concentration ($0 \le \phi \le 1$), respectively. Here, the first term stands for surface tension forces under longwave approximation. The second one is due to the energy per area for film−substrate interaction. Here

$$\kappa = \frac{\mathcal{A}}{6\pi h_e^2},\ \xi = h/h_e \tag{2}$$

where $\mathcal{A}$ is an average value of the Hamaker constant for the alloy and h_e is the equilibrium thickness ($F_{\xi}(\xi,\phi)|_{\xi=1} = 0$). To keep the discussion general, we will assume for now that F depends on both ξ and ϕ. Later in the model development, we will consider only the ξ dependence, therefore ignoring the influence of metal composition on the wetting potential. As we will see, this assumption allows us to simplify the problem considerably, while still obtaining valuable results.

The function $G(\phi)$ in the third term in eq 1 represents the bulk (or Gibbs) energy per unit volume. Its order of magnitude is given by the energy density scale

$$\mathcal{E} = \frac{k_B T}{a^3} \tag{3}$$

where k_B is the Boltzmann constant, a is a molecular length scale related to the solute, and T is the absolute temperature; typically, a is on the order of a few nanometers. For G, we use the double-well potential given by[32]

$$G(\phi) = [2\phi(\phi - 1))]^2 \tag{4}$$

It should be noted that the use of this potential corresponds to the classical Cahn−Hilliard theory of phase decomposition.[33] Finally, the last term in eq 1 stands for the energetic cost of strong gradients in the concentration, where σ is the interfacial stiffness (energy per unit length of the diffuse interface). We note that in the present model, we do not compute the temperature for an evolving film but instead consider it as a (space- and time-independent) parameter that is used for determining material properties. Careful calculations of the temperature field are discussed elsewhere.[34]

Instead of describing the problem in terms of the variables (h, ϕ), we use $h(\mathbf{x}, t)$ and the effective solute layer thickness $\psi(\mathbf{x}, t) = h(\mathbf{x}, t)\, \phi(\mathbf{x},t)$ since both are conserved quantities. The general coupled evolution equations derived within the framework of gradient dynamics[22,35] are (similar equations were also discussed in ref 21)

$$3\eta \frac{\partial h}{\partial t} + \nabla\cdot[-h^3 \nabla p - h^2 \psi \nabla \mu] = 0 \tag{5}$$

$$3\eta \frac{\partial \psi}{\partial t} + \nabla\cdot[-h^2 \psi \nabla p - (h\psi^2 + 3M\psi)\nabla \mu] = 0 \tag{6}$$

where $p = \delta\mathcal{F}/\delta h$ is the total pressure, $\mu = \delta\mathcal{F}/\delta\psi$ is the total chemical potential, η is the viscosity of the alloy, and M is the molecular mobility. Here, M and $\mathcal{E}$ are related by $\mathcal{D} = M\mathcal{E}/\eta$, where $\mathcal{D}$ is the diffusion coefficient of the alloy. This definition

https://dx.doi.org/10.1021/acs.langmuir.0c02964
Langmuir 2021, 37, 2575−2585

agrees with the Stokes−Einstein relation if $M = a^2/6\pi$.[32] Thus, the value of M can be obtained from $\mathcal{D}$, which is reported in the literature,[36] based on experimental or theoretical estimates. The only other unknown parameter is σ, which we discuss further below.

The total pressure, p, is composed of four contributions, namely,

$$p = p_{\text{cap}} + p_{\text{vdw}} + p_{\text{osm}} + p_{\text{diff}} \tag{7}$$

which correspond to the capillary, van der Waals, osmotic, and diffuse interface pressures, respectively, and are given by

$$p_{\text{cap}} = -\gamma\nabla^2 h,\ p_{\text{vdw}} = \frac{\kappa}{h_e}F_\xi - \kappa\frac{\psi}{h^2}F_\phi,$$

$$p_{\text{osm}} = \mathcal{E}\left(G - \frac{\psi}{h}G_\phi\right),$$

$$p_{\text{diff}} = \sigma\left(-\frac{2\psi}{h^3}\nabla h\nabla\psi + \frac{1}{2h^2}(\nabla\psi)^2 + \frac{3\psi^2}{2h^4}(\nabla h)^2 - \frac{\psi^2}{h^3}\nabla^2 h + \frac{\psi}{h^2}\nabla^2\psi\right) \tag{8}$$

where the subscripts denote partial derivatives, e.g., $F_\xi = \partial F/\partial\xi$. It should be commented here that for simplicity we are keeping the naming that is commonly used in the literature for solutions (such as osmotic pressure); presumably, the relevant physical mechanisms may be different for metal alloys. We note that the last pressure component can also be written in a simpler form using ϕ as an abbreviation for ψ/h

$$p_{\text{diff}} = \sigma\left(\frac{1}{2}(\nabla\phi)^2 + \frac{\phi}{h}\nabla h\cdot\nabla\phi + \phi\nabla^2\phi\right) \tag{9}$$

The total chemical potential, μ, has three contributions

$$\mu = \mu_{\text{vdw}} + \mu_{\text{osm}} + \mu_{\text{diff}} \tag{10}$$

which correspond to the van der Waals, osmotic, and diffuse interface chemical potentials, respectively, and are given by

$$\mu_{\text{vdw}} = \tfrac{\kappa}{h}F_\phi,\quad \mu_{\text{osm}} = \mathcal{E}G_\phi,$$
$$\mu_{\text{diff}} = \sigma\left(-\tfrac{\psi}{h^3}(\nabla h)^2 + \tfrac{1}{h^2}\nabla h\nabla\psi + \tfrac{\psi}{h^2}\nabla^2 h - \tfrac{1}{h}\nabla^2\psi\right) \tag{11}$$

The diffuse interface contribution can also be expressed in terms of ϕ simply as

$$\mu_{\text{diff}} = -\frac{\sigma}{h}\nabla\cdot(h\nabla\phi) \tag{12}$$

Linear Stability Analysis. An initial insight regarding the alloy stability can be reached via linear stability analysis (LSA) of an initially flat film $h = h_0$ and $\psi = \psi_0 = h_0\,\phi_0$, where ϕ_0 is the concentration of Ag. The LSA is then carried out by assuming small perturbations of h and ψ

$$h(\mathbf{r}, t) = h_0 + h_1\exp(\mathbf{ik}\cdot\mathbf{r} + \omega t),$$
$$\psi(\mathbf{r}, t) = \psi_0 + \psi_1\exp(\mathbf{ik}\cdot\mathbf{r} + \omega t) \tag{13}$$

where $h_1 \ll h_0$, $\psi_1 \ll \psi_0$, $\mathbf{k} = (k_x, k_y)$ is the wavenumber, $\mathbf{r} = (x, y)$, and ω is the growth rate. By linearizing eq 5, we obtain a system of equations for h_1 and ψ_1 in the form

$$a_{11}h_1 + a_{12}\psi_1 = 0,\ a_{21}h_1 + a_{22}\psi_1 = 0 \tag{14}$$

where

$$a_{11} = \omega - \omega_{\text{h}} + \phi_0\frac{\kappa h_0}{3\eta}k^2(hF_\phi^0 - F_{\xi\phi}^0) \tag{15}$$

$$a_{12} = -\frac{\kappa h_0}{3\eta}k^2(hF_\phi^0 - F_{\xi\phi}^0) \tag{16}$$

$$a_{21} = \phi_0(\omega_\phi - \omega_{\text{h}}) + \phi_0\frac{\kappa M}{3\eta h_0}k^2[(\phi_0 - 3D)hF_\phi^0 + 3DhF_{\phi\phi}^0 - (3D - \phi_0)F_{\xi\phi}^0] \tag{17}$$

$$a_{22} = \omega - \omega_\phi - \phi_0\frac{\kappa h_0}{3\eta}k^2\left(hF_\phi^0 - F_{\xi\phi}^0 - 3\frac{M}{h_0^2}hF_{\phi\phi}^0\right) \tag{18}$$

and

$$\omega_{\text{h}} = -\frac{\gamma h_0^3 k^2}{3\eta}\left(k^2 + \frac{\kappa}{\gamma h_e^2}F_{\xi\xi}^0\right),\ \omega_\phi = -\mathcal{D}\phi_0 k^2\left(\frac{\sigma k^2}{\mathcal{E}} + G_{\phi\phi}^0\right) \tag{19}$$

Here, the superscript 0 in F and G stands for the evaluation at $h = h_0$ and $\phi = \phi_0$. If F does not depend on ϕ, all of the terms in the parentheses become zero and then we find two independent dispersion relations for the growth rate, namely, $\omega = \omega_{\text{h}}$ and $\omega = \omega_\phi$. Both eigenvalues are real in this case, in accordance with previous results of the linear approximation of the gradient dynamics formulation.[37] The corresponding maximum growth rates are $\omega_{\text{m,h}} = \omega_{\text{h}}(k_{\text{m,h}})$ and $\omega_{\text{m},\phi} = \omega_\phi(k_{\text{m},\phi})$, where

$$\omega_{\text{m,h}} = \frac{h_0^3}{12\eta\gamma}\left(\frac{\kappa F_{\xi\xi}^0}{h_e}\right)^2 \quad \text{at} \quad k_{\text{m,h}} = \sqrt{-\frac{\kappa F_{\xi\xi}^0}{2\gamma h_e}} \tag{20}$$

$$\omega_{\text{m},\phi} = \frac{\mathcal{D}\phi_0\mathcal{E}}{4\sigma}(G_{\phi\phi}^0)^2 \quad \text{at} \quad k_{\text{m},\phi} = \sqrt{-\frac{\mathcal{E}G_{\phi\phi}^0}{2\sigma}} \tag{21}$$

From now on, we only consider the ξ-dependence of F; exploring the influence of ϕ dependence is left for future work. As seen above, we then have linearly independent dewetting and decomposition processes. Thus, we assume the usual power-law dependence of F on ξ, namely, the Frumkin−Derjaguin model;[38−40] see also ref 41 regarding the review of various forms of the disjoining pressure. We implement here a combination of power laws

$$F(\xi) = \frac{\xi^{1-n}}{n-1} - \frac{\xi^{1-m}}{m-1} \tag{22}$$

For $n > m$ (see ref 3 more details regarding appropriate interfacial potentials for metals), we find that films are unstable for $h_e < h_0\,(m/n)^{1/(n-m)}$ (see eq 19 for ω_{h}). Here, we use $(n, m) = (3, 2)$.[42] Regarding ω_ϕ in eq 19, note that for the assumed double-well potential, phase-separation instability occurs for $0.21 < \phi_0 < 0.79$.

Material Parameters. Next, we discuss the relevant material parameters, mainly accounting for their dependence on temperature, T. Including this dependence turns out to be crucial for the purpose of developing direct comparison with the experiments. The reference values at melting are given in Table 1 in the Supporting Information.

To summarize our approach, we use the temperature dependence of the material parameters from the literature when possible (such dependence can be found in precise terms for surface tension and viscosity). For the remaining parameters,

https://dx.doi.org/10.1021/acs.langmuir.0c02964
Langmuir 2021, 37, 2575−2585

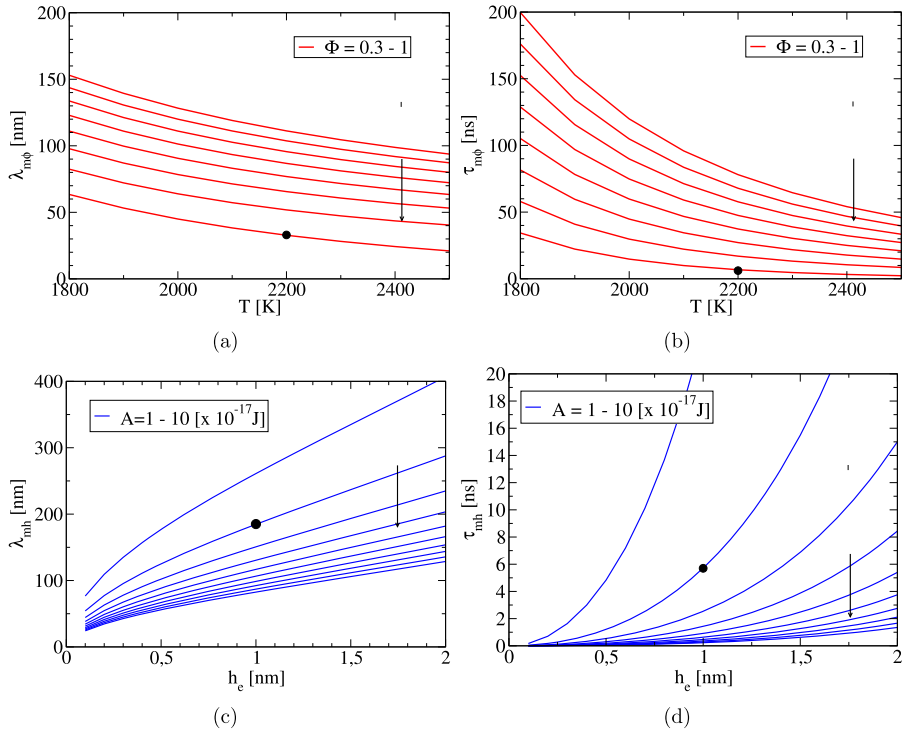

Figure 7. (a) Characteristic length and (b) characteristic time of the concentration instability as a function of temperature T for given values of the Girifalco−Goods coefficient, Φ. The arrow shows the direction of Φ increase. (c) Characteristic length and (d) characteristic time of the thickness instability as a function of h_e for parametrically specified values of the Hamaker constant $\mathcal{A}$. The arrow shows the direction of $\mathcal{A}$ increase. In all cases, the black points indicate the chosen values for the simulations: (a) $\lambda_{m,\phi}$ = 33 nm, (b) $\tau_{m,\phi}$ = 6.1 ns, (c) $\lambda_{m,h}$ = 185 nm, and (d) $\tau_{m,h}$ = 5.7 ns.

which are not exactly known, we use the experimental results as a guide and then confirm that the obtained values of the considered parameters are reasonable in the order-of-magnitude sense when compared to the literature. We note that we will simplify the discussion using a representative value of the temperature, without considering its temporal or spatial dependence; for the remaining presentation, T will refer to this representative temperature value.

To start with, we take into account the dependence of η and γ on T and assume that the density, ρ, is constant; the parameters used for each metal are given in Table 1 in the Supporting Information. The liquid metals' viscosity is assumed to depend on T following the Arrhenius law

$$\eta = \eta_m \exp\left[\frac{E_a}{R}\left(\frac{1}{T} - \frac{1}{T_m}\right)\right] \tag{23}$$

where $R = k_B N_a$, with N_a being the Avogadro number, E_a is the activation energy, and η_m is the viscosity at a melting point of temperature T_m.[43]

Regarding the surface tension, we use the following relationship with viscosity[43,44]

$$\gamma = \gamma_m \frac{\eta}{\eta_m}\sqrt{\frac{T}{T_m}} \tag{24}$$

where γ_m is the surface tension at T_m. Moreover, we also take into account the dependence of diffusivity, $\mathcal{D}$, on T as[36]

$$\mathcal{D} = \mathcal{D}_0\left(\frac{T}{T_0}\right)^{3/2} \tag{25}$$

where $\mathcal{D}_0$ is a reference value at T_0 = 1234 K. We treat the Hamaker constant as temperature-independent due to the lack of any explicit data on the possible dependence of this quantity on temperature. Accurate information about the contact angle variation on temperature, if available, could be used for this purpose. However, we are not aware that such measurements have been carried out for melted alloys.

The parameters of the alloy are then given by the weighted average

$$\theta = \phi_0\theta_{Ag} + (1 - \phi_0)\theta_{Ni} \tag{26}$$

where θ stands for $\mathcal{A}$, η, γ, and $\mathcal{D}$. Note that we do not consider variations of material parameters with local film composition, which may be spatially and temporally dependent.

The value of the interfacial stiffness, σ, for the considered alloy is not precisely known. One approach to estimate it is to assume that the effective thickness of the diffuse interface between the phases is on the order of a and that σ is related to the interfacial tension between Ag and Ni phases, γ_{AgNi}, as

$$\sigma = a\,\gamma_{AgNi}$$

Here, the value of γ_{AgNi} can be approximated by means of the Girifalco−Good formula[45]

$$\gamma_{AgNi} = \gamma_{Ag} + \gamma_{Ni} - 2\Phi(\gamma_{Ag}\gamma_{Ni})^{1/2} \tag{27}$$

where Φ is a constant close to one for most of the liquids but not exactly known.

Finally, we note that the values for h_e and $\mathcal{A}$ cannot be found in the literature for our combination of the alloy and substrate, and we could only expect a similar order of magnitude as for simple metals. Therefore, we obtain these four parameters, namely, T, Φ, h_e, and $\mathcal{A}$, that we do not precisely know from the

https://dx.doi.org/10.1021/acs.langmuir.0c02964
Langmuir 2021, 37, 2575−2585

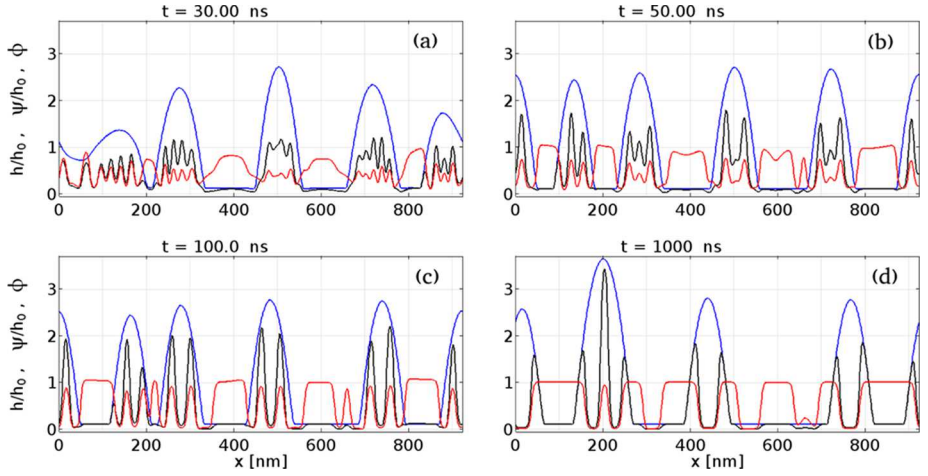

Figure 8. Time evolution of h/h_0 (blue), ψ/h_0 (black), and $\phi = \psi/h$ (red) for a film of thickness $h_0 = 10$ nm and Ag concentration $\phi_0 = 0.4$ in a domain $L = 5\lambda_{m,h} = 956.2$ nm: (a) $t = 30$ ns, (b) $t = 50$ ns, (c) $t = 100$ ns, and (d) $t = 1000$ ns. See Supporting Information Movie-2D for animations.

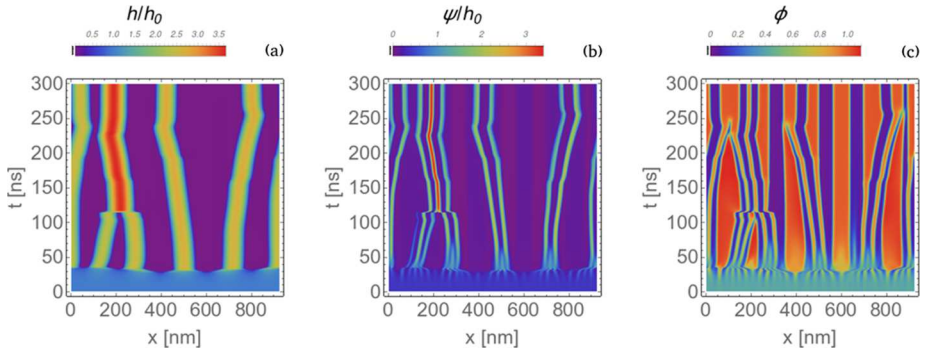

Figure 9. Space−time plots showing evolution of the patterns from Figure 8 (for early times). As in Figure 8, ϕ corresponds to Ag concentration. The kinks that are visible around times ∼220−230 ns are discussed in the text, see also Supporting Information Movie-2D for animations.

requirement that they lead to values of the characteristic times and lengths for the linear instability of both thickness, h, and concentration, ϕ, in agreement with those observed in the experiments. For definitiveness and brevity, here, we focus discussion on the 10 nm thick films only.

We first consider the ϕ instability and discuss the behavior of both $\lambda_{m,\phi} = 2\pi/k_{m,\phi}$ and $\tau_{m,\phi} = 1/\omega_{m,\phi}$ as a function of T for given values of Φ. Figure 7a,b shows the dependence of these quantities on T and Φ. These plots and the experimental observations for the relevant length and time scales (approximate values extracted from Figure 4a) lead to the choice of $T = 2200$ K and $\Phi = 1$ (black points in Figure 7a,b). Finally, assuming that in the experiment we have $T = 2200$ K and $\phi_0 = 1.0$, we obtain $\eta_{Ni} = 2.32$ mPa s, $\gamma_{Ni} = 0.981$ N/m and $\eta_{Ag} = 1.50$ mPa s, $\gamma_{Ag} = 0.475$ N/m.

With the representative value of temperature now determined, we consider the length scale $\lambda_{m,h} = 2\pi/k_{m,h}$ and time $\tau_{m,h} = 1/\omega_{m,h}$ as a function of h_e for given values of $\mathcal{A}$. Figure 7c,d and the experimental observations shown in Figure 6 lead to the choice $h_e = 1$ nm and $\mathcal{A} = 2 \times 10^{-17}$ J (black points in Figure 7c,d). We point out that the choice of appropriate value for h_e is also governed by practical considerations: the simulations that will be discussed in what follows are difficult to carry out for very small values of h_e; for this reason, we chose $h_e = 1$ nm, although the real value may be smaller, see ref 42.

With the parameters specified, we now consider a film of thickness $h_0 = 10$ nm, for which we find $1/\omega_{m,h} \approx 5.7$ ns, $\lambda_{m,h} \approx 185$ nm, $1/\omega_{m,\phi} \approx 6.1$ ns, and $\lambda_{m,\phi} \approx 33$ nm. We note that the phase separation develops for much smaller wavelengths than the thickness instability, while the time scales of the two instabilities are comparable.

Nonlinear Numerical Simulations. To discuss the nonlinear stage of the instability development, we carry out fully nonlinear time-dependent simulations of the evolution equations (eqs 5 and 6) using the COMSOL Multiphysics package (see Sections 2 and 3 in the Supporting Information for details). We take as a base state a flat film specified by h_0, ϕ_0 with periodic boundary conditions at the domain boundaries. First, we consider the two-dimensional (2D) problem, with the initially perturbed base state as follows

$$h(x, t = 0) = h_0\left[1 + \sum_{i=1}^{N} (A_i \cos(ik_0x) + B_i \sin(ik_0x))\right] \quad (28)$$

$$\psi(x, t = 0) = \psi_0\left[1 + \sum_{i=1}^{N} (C_i \cos(ik_0x) + D_i \sin(ik_0x))\right] \quad (29)$$

where $0 \le x \le L$; $k_0 = 2\pi/L$; and A_i, B_i, C_i, and D_i, are random numbers uniformly distributed in $(-\epsilon, \epsilon)$ and of zero mean. We use $\epsilon = 0.001$ and $N = 400$.

Figure 8 shows that the initial stage of the evolution is consistent with the LSA, as expected. Regarding comparison with the experimental results, we consider separately the film (free surface) instability and phase separation. In the context of

https://dx.doi.org/10.1021/acs.langmuir.0c02964
Langmuir 2021, 37, 2575−2585

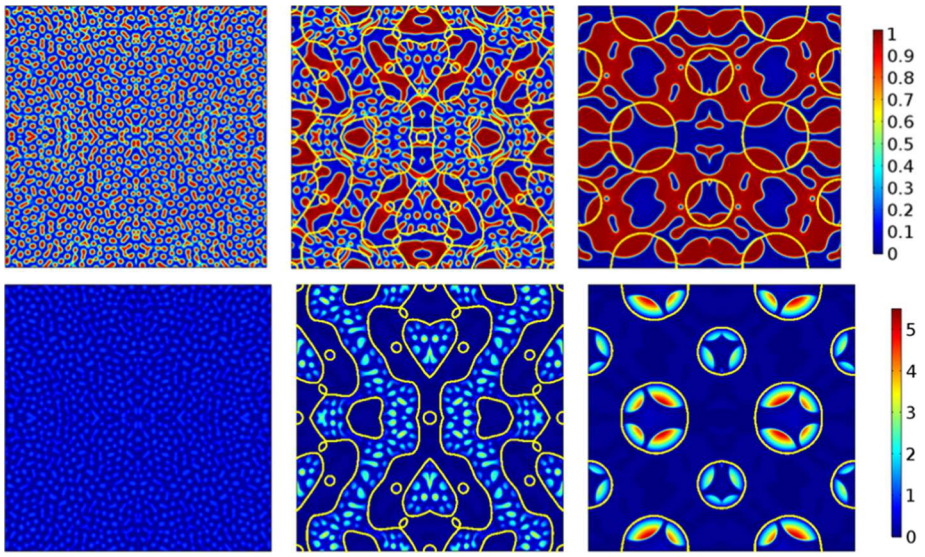

Figure 10. Evolution of (top) $\phi = \psi/h$ and (bottom) ψ/h_0 (h_0 = 10 nm and ϕ_0 = 0.4) for (left to right) t = 40, 80, and 700 ns. The yellow solid curves show the drop border (level line for $h = 1.5\ h_e$). The linear dimension is 6 $\lambda_{m,h}$, twice as large as the actual computational domain size. See Supporting Information Movie-3D-phi and Movie-3D-psi for animations.

film instability, we find that the typical time scale for formation of drops is less than 30 ns (blue lines in Figure 8), consistent with the experimental results shown in Figure 2. The emerging length scales are comparable as well, viz., Figure 6b—the peak of the histogram showing particle distribution is at 200 nm, close to the average distance between the drops in simulations. Focusing now on the phase instability, we note that in the experiments the phase separation occurs on the spatial scale of 40−50 nm, see Figure 4a after a single pulse, with some coarsening for later times, see the same figure after five pulses. Similar length scales can be observed in Figure 8, see black (ψ) or red (ϕ) lines. The time scale on which phase separation occurs in the experiments, less than 1 pulse duration (20 ns), is again consistent with the results shown in Figure 8. We note that the metal distribution within the formed drops varies, viz., Figure 8d, similarly to that in the experiments, viz., Figure 3. Further work including more elaborate modeling may be needed however to reach more precise and definite answers regarding the expected distribution of the two phases and whether there is a particular final preferred structure.

Figure 9 shows the space−time plot of the instability development, allowing us to visualize more clearly the nonlinear stages of instability development. As already anticipated by the results shown in Figure 8, for later times, we observe the formation of drops and, in parallel, phase separation and slow coarsening (one coarsening event could be seen in Figure 9 around time 110 ns, when two large drops merge at $x \sim 200$ nm). Perhaps unexpected dynamics could be observed around times ~220−230 ns, where kinks are visible in the space−time profiles. Careful inspection of the animation (see Supporting Information, Movie-2D) shows that the source of these kinks appears to be a nonlinear interaction between translation of the already formed drops and evolving concentration field. A more detailed analysis of this behavior is left for future work.

We have also carried out simulations for different values of ϕ_0 (0.2, 0.5, and 0.7) and h_0 (20 and 30 nm) with no qualitative differences in the final results. We note that the pattern shown in Figures 8 and 9 appears to be still evolving (even if very slowly), leading possibly to further coarsening but on a much longer time scale. To put these results in context, the reader is referred to ref 20 for future discussion regarding steady states for films and drops with phase separation but without dewetting effects and to refs 46, 47 for discussion of compound drops, albeit in a different setting.

Next, we proceed by considering the 3D problem. Due to computational limitations inherent to the present simulation method, we use a relatively small square domain of linear dimension $L = 3\lambda_{m,h}$. The initial condition is a simple 3D extension of the 2D one, with

$$h(x, y, t = 0) = h_0\left[1 + \sum_{i=1}^{N}\sum_{j=1}^{N}(A_{i,j}\cos(ik_0x)\cos(jk_0y) + B_{i,j}\sin(ik_0x)\sin(jk_0y))\right] \quad (30)$$

and a corresponding expression for $\psi(x, y, 0)$ (N = 100 here). Figure 10 (see also the animations in the Supporting Information) illustrates that the evolution is in general terms similar to the one observed in 2D and consistent with the experiment. The two types of instabilities evolve in parallel, with drops forming while the concentration field is still evolving. It should be noted that while early stages of the instability may not be influenced strongly by the domain size, the later stages might be since nonlinearity often leads to an energy cascade from larger to smaller wavelengths; the lack of such longer length scales in the present situation may play a role. Still, we expect the patterns shown in Figure 10 to be representative of the ones that would be obtained in larger domains.

CONCLUSIONS

Two experimental setups, considering thin alloy films evolving either on thin supporting membranes or on bulk substrates, have allowed us to obtain simultaneous information about two instability mechanisms: breakup of liquid alloy films into drops and chemical instability, involving phase separation of constitutive metals. These results have guided further develop-

https://dx.doi.org/10.1021/acs.langmuir.0c02964
Langmuir 2021, 37, 2575−2585

ment of the theoretical model based on the longwave Cahn−Hilliard formulation governing phase separation, asymptotically consistent model describing free surface evolution, and utilizing disjoining pressure describing destabilizing forces driving film breakup. The model that we have presented may be considered as a first step in developing a more complete approach that would include a number of aspects that have not been considered in detail (or not at all) in the present work. These include, in particular, coupling of the present model with self-consistent computations of the temporally and spatially dependent temperature field, as well as including the fact that the metal/substrate interaction forces, modeled by the disjoining pressure formulation, may depend on the alloy composition.

Despite the implemented simplifications, we have shown that the current model can be used to accurately describe the experimental results. The model therefore provides a basic setup to help devise novel experimental setups directing the coupled free surface and phase-separation instabilities to produce particles of desired properties. We hope that the presented work will encourage further research that will provide even more precise information about the liquid-phase evolution of immiscible alloy films toward bimetallic functional nanoparticle assemblies.

■ ASSOCIATED CONTENT

Supporting Information

The Supporting Information is available free of charge at https://pubs.acs.org/doi/10.1021/acs.langmuir.0c02964.

Animation of the evolution shown in Figure 8 (Movie-2D) (MPG)

Animation of the evolution shown in the top row of Figure 10 (Movie-3d-phi) (MPG)

Animation of the evolution shown in the bottom row of Figure 10 (Movie-3d-psi) (MPG)

Finite-element method (FEM) temperature calculations; nondimensional formulation of the governing equations; description of simulation methods; and additional results (PDF)

■ AUTHOR INFORMATION

Corresponding Author

Lou Kondic − *Department of Mathematical Sciences, New Jersey Institute of Technology, Newark, New Jersey 07102, United States;* orcid.org/0000-0001-6966-9851; Email: kondic@njit.edu

Authors

Javier A. Diez − *CIFICEN-CONICET-CICPBA, Instituto de Física Arroyo Seco, Universidad Nacional del Centro de la Provincia de Buenos Aires, 7000 Tandil, Argentina*

Alejandro G. González − *CIFICEN-CONICET-CICPBA, Instituto de Física Arroyo Seco, Universidad Nacional del Centro de la Provincia de Buenos Aires, 7000 Tandil, Argentina;* orcid.org/0000-0002-4710-6414

David A. Garfinkel − *Department of Materials Science & Engineering, University of Tennessee, Knoxville, Tennessee 37996, United States; Center for Nanophase Materials Science, Oak Ridge National Laboratory, Oak Ridge, Tennessee 37831, United States;* orcid.org/0000-0002-7593-1868

Philip D. Rack − *Department of Materials Science & Engineering, University of Tennessee, Knoxville, Tennessee 37996, United States; Center for Nanophase Materials Science, Oak Ridge National Laboratory, Oak Ridge, Tennessee 37831, United States;* orcid.org/0000-0002-9964-3254

Joseph T. McKeown − *Materials Science Division, Lawrence Livermore National Laboratory, Livermore, California 94550, United States*

Complete contact information is available at: https://pubs.acs.org/10.1021/acs.langmuir.0c02964

Notes

The authors declare no competing financial interest.

■ ACKNOWLEDGMENTS

The authors acknowledge support by NSF Grants CBET-1603780 (D.A.G. and P.D.R.) and CBET-1604351 and DMS-1815613 (L.K.). All of the authors acknowledge that scanning electron microscopy was conducted at the Center for Nanophase Materials Sciences, which is a DOE Office of Science User Facility. J.A.D. and A.G.G. acknowledge support from Consejo Nacional de Investigaciones Científicas y Técnicas (CONICET, Argentina) and Agencia Nacional de Promoción Científica y Tecnológica (ANPCyT, Argentina) under Grant PICT 1067/2016 Work at Lawrence Livermore National Laboratory was performed under the auspices of the U.S. Department of Energy under Contract No. DE-AC52-07NA27344.

■ REFERENCES

(1) Hughes, R. A.; Menumerov, E.; Neretina, S. When lithography meets self-assembly: a review of recent advances in the directed assembly of complex metal nanostructures on planar and textured surfaces. *Nanotechnology* **2017**, *28*, No. 282002.

(2) Makarov, S. V.; Milichko, V. A.; Mukhin, I. S.; Shishkin, I. I.; Zuev, D. A.; Mozharov, A. M.; Krasnok, A. E.; Belov, P. A. Controllable femtosecond laser-induced dewetting for plasmonic applications. *Laser Photonics Rev.* **2016**, *10*, 91.

(3) Kondic, L.; González, A. G.; Diez, J. A.; Fowlkes, J. D.; Rack, P. Liquid-State Dewetting of Pulsed-Laser-Heated Nanoscale Metal Films and Other Geometries. *Annu. Rev. Fluid Mech.* **2020**, *52*, 235.

(4) Ruffino, F.; Grimaldi, M. G. Nanostructuration of Thin Metal Films by Pulsed Laser Irradiations: A Review. *Nanomaterials* **2019**, *9*, No. 1133.

(5) Bischof, J.; Scherer, D.; Herminghaus, S.; Leiderer, P. Dewetting modes of thin metallic films: Nucleation of holes and spinodal dewetting. *Phys. Rev. Lett.* **1996**, *77*, No. 1536.

(6) Yadavali, S.; Krishna, H.; Kalyanaraman, R. Morphology transitions in bilayer spinodal dewetting systems. *Phys. Rev. B* **2012**, *85*, No. 235446.

(7) Khenner, M.; Yadavali, S.; Kalyanaraman, R. Formation of organized nanostructures from unstable bilayers of thin metallic liquids. *Phys. Fluids* **2011**, *23*, No. 122105.

(8) Garfinkel, D. A.; Pakeltis, G.; Tang, N.; Ivanov, I. N.; Fowlkes, J. D.; Gilbert, D. A.; Rack, P. D. Optical and Magnetic Properties of Ag-Ni Bimetallic Nanoparticles Assembled via Pulsed Laser-Induced Dewetting. *ACS Omega* **2020**, *5*, 19285.

(9) Mao, S.; Kuldinow, D.; Haataja, M. P.; Kosmrlj, A. Phase behavior and morphology of multicomponent liquid mixtures. *Soft Matter* **2019**, *15*, 1297.

(10) Schnedlitz, M.; Fernandez-Perea, R.; Knez, D.; Lasserus, M.; Schiffmann, A.; Hofer, F.; Hauser, A. W.; de Lara-Castells, M. P.; Ernst, W. E. Effects of the Core Location on the Structural Stability of Ni-Au Core Shell Nanoparticles. *J. Phys. Chem. C* **2019**, *123*, 20037−20043.

(11) Sachan, R.; Yadavali, S.; Shirato, N.; Krishna, H.; Ramos, V.; Duscher, G.; Pennycook, S. J.; Gangopadhyay, A. K.; Garcia, H.; Kalyanaraman, R. Self-organized bimetallic Ag−Co nanoparticles with tunable localized surface plasmons showing high environmental stability and sensitivity. *Nanotechnology* **2012**, *23*, No. 275604.
(12) Sachan, R.; Malasi, A.; Ge, J.; Yadavali, S.; Krishna, H.; Gangopadhyay, A.; Garcia, H.; Duscher, G.; Kalyanaraman, R. Ferroplasmons: Intense Localized Surface Plasmons in Metal-Ferromagnetic Nanoparticles. *ACS Nano* **2014**, *8*, 9790.
(13) Cahn, J. W.; Hilliard, J. E. Free energy of a nonuniform system. 1. Interfacial free energy. *J. Chem. Phys.* **1958**, *28*, 258.
(14) Fischer, H. P.; Maass, P.; Dieterich, W. Novel Surface Modes in Spinodal Decomposition. *Phys. Rev. Lett.* **1997**, *79*, No. 893.
(15) Fischer, H. P.; Maass, P.; Dieterich, W. Diverging time and length scales of spinodal decomposition modes in thin films. *Europhys. Lett.* **1998**, *42*, 49−54.
(16) Hohenberg, P. C.; Halperin, B. I. Theory of dynamic critical phenomena. *Rev. Mod. Phys.* **1977**, *49*, No. 435.
(17) Anderson, D. M.; McFadden, G. B.; Wheeler, A. A. Diffuse-interface methods in fluid mechanics. *Annu. Rev. Fluid Mech.* **1998**, *30*, 139−165.
(18) Thiele, U.; Madruga, S.; Frastia, L. Decomposition driven interface evolution for layers of binary mixtures. I. Model derivation and stratified base states. *Phys. Fluids* **2007**, *19*, No. 122106.
(19) Madruga, S.; Thiele, U. Decomposition driven interface evolution for layers of binary mixtures. II. Influence of convective transport on linear stability. *Phys. Fluids* **2009**, *21*, No. 062104.
(20) Bribesh, F. A. M.; Frastia, L.; Thiele, U. Decomposition driven interface evolution for layers of binary mixtures: III. Two-dimensional steady film states. *Phys. Fluids* **2012**, *24*, No. 062109.
(21) Náraigh, L. Ó.; Thiffeault, J.-L. Nonlinear dynamics of phase separation in thin films. *Nonlinearity* **2010**, *23*, 1559−1583.
(22) Thiele, U.; Todorova, D. V.; Lopez, H. Gradient Dynamics Description for Films of Mixtures and Suspensions: Dewetting Triggered by Coupled Film Height and Concentration Fluctuations. *Phys. Rev. Lett.* **2013**, *111*, No. 117801.
(23) Wu, Y.; Liu, C.; Moore, T. M.; Magel, G. A.; Garfinkel, D. A.; Camden, J. P.; Stanford, M. G.; Duscher, G.; Rack, P. R. Exploring Photothermal Pathways via in Situ Laser Heating in the Transmission Electron Microscope: Recrystallization, Grain Growth, Phase Separation, and Dewetting in $Ag_{0.5}Ni_{0.5}$ Thin Films. *Microsc. Microanal.* **2018**, *24*, 647.
(24) McKeown, J. T.; Roberts, N. A.; Fowlkes, J. D.; Wu, Y.; LaGrange, T.; Reed, B. W.; Campbell, G. H.; Rack, P. D. Real-Time Observation of Nanosecond Liquid-Phase Assembly of Nickel Nanoparticles via Pulsed-Laser Heating. *Langmuir* **2012**, *28*, 17168.
(25) McKeown, J. T.; Wu, Y.; Fowlkes, J. D.; Rack, P. D.; Campbell, G. H. Simultaneous In-Situ Synthesis and Characterization of Co-Cu Core-Shell Nanoparticle Arrays. *Adv. Mater.* **2015**, *27*, 1060−1065.
(26) Reiter, G. Dewetting of thin polymer films. *Phys. Rev. Lett.* **1992**, *68*, No. 75.
(27) Seemann, R.; Herminghaus, S.; Jacobs, K. Dewetting patterns and molecular forces: a reconciliation. *Phys. Rev. Lett.* **2001**, *86*, No. 5534.
(28) Seemann, R.; Herminghaus, S.; Neto, C.; Schlagowski, S.; Podziodesek, D.; Konrad, R.; Mantz, H.; Jacobs, K. Dynamics and structure formation in thin polymer melt films. *J. Phys.: Condens. Matter* **2005**, *17*, S267.
(29) Engelnkemper, S.; Wilczek, M.; Gurevich, S. V.; Thiele, U. Morphological transitions of sliding drops: Dynamics and bifurcations. *Phys. Rev. Fluids* **2016**, *1*, No. 073901.
(30) Sarika, C. K.; Tomar, G.; Basu, J. K.; Thiele, U. Bimodality and re-entrant behaviour in the hierarchical self-assembly of polymeric nanoparticles. *Soft Matter* **2015**, *11*, 8975−8980.
(31) Sarika, C. K.; Tomar, G.; Basu, J. K. Pattern formation in thin films of polymer solutions: theory and simulations. *J. Chem. Phys.* **2016**, *144*, No. 024902.
(32) Thiele, U. Note on thin film equations for solutions and suspensions. *Eur. Phys. J. Spec. Top.* **2011**, *197*, 213−220.
(33) Cahn, J. W. Phase separation by spinodal decomposition in isotropic systems. *J. Chem. Phys.* **1965**, *42*, 93.
(34) Allaire, R.; Cummings, L. J.; Kondic, L. On efficient asymptotic modelling of thin films on thermally conductive substrates. *J. Fluid Mechanics*, in press.
(35) Todorova, D. V. Modelling of Dynamical Effects Related to the Wettability and Capillarity of Simple and Complex Liquids. Ph.D. Thesis, Loughborough University, 2013.
(36) Bhat, B. N. *Solute Diffusion in Liquid Metals*, Technical Report; NASA Marshall Space Flight Center: AL, 1973.
(37) Thiele, U.; Archer, A. J.; Plapp, M. Thermodynamically consistent description of the hydrodynamics of free surfaces covered by insoluble surfactants of high concentration. *Phys. Fluids* **2012**, *24*, No. 102107.
(38) Frumkin, A. N. Phenomena of wetting and adhesion of bubbles. *Zh. Fiz. Khim.* **1938**, *12*, 337.
(39) Derjaguin, B.; Landau, L. Theory of the stability of strongly charged lyophobic sols and of the adhesion of strongly charged particles in solutions of electrolytes. *Acta Phys. Chem. USSR* **1941**, *14*, 633.
(40) Churaev, N. V. Contact angles and surface forces. *Adv. Colloid Interface Sci.* **1995**, *58*, 87−118.
(41) Teletzke, G.; Davis, H.; Scriven, L. Wetting hydrodynamics. *Rev. Phys. Appl.* **1988**, *23*, No. 989.
(42) González, A. G.; Diez, J. A.; Wu, Y.; Fowlkes, J. D.; Rack, P. D.; Kondic, L. Instability of liquid Cu films on a SiO_2 substrate. *Langmuir* **2013**, *29*, 9378.
(43) Battezzati, L.; Greer, A. L. The viscosity of liquid metals and alloys. *Acta Metall.* **1989**, *37*, 1791.
(44) Egry, I.; Lohöfer, G.; Sauerland, S. Surface tension and viscosity of liquid metals. *J. Non-Cryst. Solids* **1993**, *156−158*, 830−832.
(45) Girifalco, L. A.; Good, R. J. A theory for the estimation of surface and interfacial energies I: Derivation and application to interfacial tension. *J. Phys. Chem. A* **1957**, *61*, 904−909.
(46) Mahadevan, L.; Adda-Bedia, M.; Pomeau, Y. Four-phase merging in sessile compound drops. *J. Fluid Mech.* **2002**, *451*, 411−420.
(47) Neeson, M. J.; Tabor, R. F.; Grieser, F.; Dagastine, R. R.; Chan, D. Y. C. Compound sessile drops. *Soft Matter* **2012**, *8*, 11042−11050.

https://dx.doi.org/10.1021/acs.langmuir.0c02964
Langmuir 2021, 37, 2575−2585